

# Gas dynamics in high-luminosity polarized $^3\text{He}$ targets using diffusion and convection.

\*\*\*PENULTIMATE DRAFT\*\*\*

P.A.M. Dolph,<sup>1,\*</sup> J. Singh,<sup>1,2</sup> T. Averett,<sup>3</sup> A. Kelleher,<sup>3,4</sup> K. Mooney,<sup>1</sup>  
V. Nelyubin,<sup>1</sup> W.A. Tobias,<sup>1</sup> B. Wojtsekhowski,<sup>5</sup> and G.D. Cates<sup>1</sup>

<sup>1</sup>*University of Virginia, Charlottesville, VA 22903*

<sup>2</sup>*Argonne National Lab, Argonne, IL 60439*

<sup>3</sup>*College of William and Mary, Williamsburg, VA 23187*

<sup>4</sup>*Massachusetts Institute of Technology 02139*

<sup>5</sup>*Thomas Jefferson National Accelerator Facility, Newport News, VA 23606*

(Dated: May 5, 2011)

The dynamics of the movement of gas is discussed for two-chambered polarized  $^3\text{He}$  target cells of the sort that have been used successfully for many electron scattering experiments. A detailed analysis is presented showing that diffusion presents a limiting factor in target performance, particularly as these targets are run at increasingly high luminosities. Measurements are presented on a new prototype polarized  $^3\text{He}$  target cell in which the movement of gas is due largely to convection instead of diffusion. NMR tagging techniques have been used to visualize the gas flow, showing velocities along a cylindrically-shaped target of between 5 – 80 cm/min. The new target design addresses one of the principle obstacles to running polarized  $^3\text{He}$  targets at substantially higher luminosities while simultaneously providing new flexibility in target geometry.

## I. INTRODUCTION

Nuclear-polarized  $^3\text{He}$  has proven to be useful in a number of different areas of research. In electron scattering, polarized  $^3\text{He}$  provides a means for studying spin-dependent interactions involving neutrons. This is because, to first approximation, a  $^3\text{He}$  nucleus is comprised of a pair of protons whose spins are paired, and a single neutron that accounts for most of the nuclear spin. An important early example of the use of polarized  $^3\text{He}$  in electron scattering came during an experiment to measure the internal spin structure of the neutron at the Stanford Linear Accelerator Center (SLAC), E142 [1]. Polarized  $^3\text{He}$  has also been used to measure the electric form factor of the neutron  $G_E^n$ , including a recent experiment at Jefferson Laboratory in Newport News, Va (JLab)[2]. Important applications of polarized  $^3\text{He}$  have included, for example, its use as a neutron polarizer [3], and, together with polarized  $^{129}\text{Xe}$ , providing a source of signal for magnetic resonance imaging [4, 5].

There are two predominant techniques by which nuclear polarization is produced in  $^3\text{He}$ . In one technique, often known as metastability exchange optical pumping (MEOP), metastable states of  $^3\text{He}$  are optically pumped directly, and subsequently transfer their polarization to other ground-state  $^3\text{He}$  nuclei during collisions [6, 7]. In a second technique, known as spin-exchange optical pumping (SEOP), a vapor of alkali-metal atoms is optically pumped, and again transfer their polarization to  $^3\text{He}$  nuclei during subsequent collisions [8–10]. An important difference between the two techniques is that MEOP is performed at pressures that are quite low, around a few

Torr, whereas SEOP is often done at pressures as high as around ten atmospheres. When a high-density is required, a target based on MEOP inevitably involves a compressor of some sort. In contrast, high-density targets based on SEOP typically utilize a sealed glass cell with no moving parts and hence have an advantage from the perspective of simplicity. In considering relative merits, however, one also needs to consider the speed with which the gas is polarized. Here targets based on MEOP have done quite well, with a recent target at the Mainz Microtron reporting a polarization rate of 2 bar liters per hour[11]. In short, both techniques for polarizing  $^3\text{He}$  have been quite successful.

For electron-scattering experiments in which  $^3\text{He}$  is polarized using SEOP, the targets typically utilize a sealed glass cell with two distinct chambers: a “pumping chamber” in which the gas is polarized, and a “target chamber” through which the electron beam passes (see Fig. 1). This design ensures that ionization due to the electron beam does not adversely affect the optical pumping process, as well as providing in the pumping chamber a geometry that lends itself well to illumination with lasers. The two chambers are connected by a “transfer tube”, and gas that is polarized in the pumping chamber migrates into the target chamber largely by diffusion.

Several conditions need to be met in targets with designs such as that shown in Fig. 1 in order to maintain high polarization. First, the rate at which the  $^3\text{He}$  is polarized must be relatively fast compared to the rate at which the  $^3\text{He}$  is depolarized. While this is true in all work involving SEOP, it is of particular significance when considering depolarization of the  $^3\text{He}$  due to the electron beam. There are also issues having to do with polarization dynamics that are unique to the two-chamber design. As has been pointed out by Chupp *et al.*[12], it is important that diffusion between the two chambers is rapid compared to other time constants in the system.

---

\*pad8c@virginia.edu

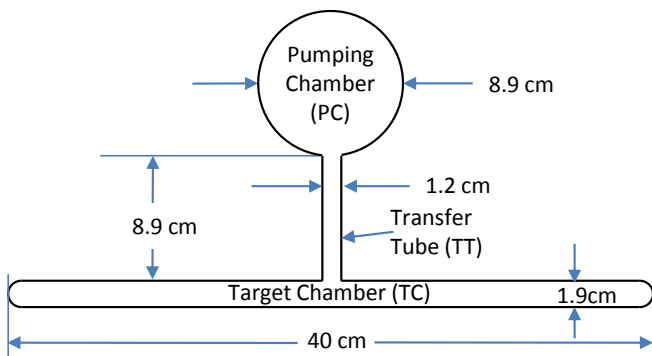


FIG. 1: Shown is the geometry of a two-chambered glass cell used for polarized  $^3\text{He}$  targets. The dimensions shown are typical of those used in a recent JLab experiment to measure the electric form factor of the neutron [2].

As we will show in detail, a matter of special importance is maximizing the ratio of the diffusion rate to the relaxation rate that is specific to the target chamber. Put differently, it is critical that the polarized gas in the target chamber is replenished much faster than it is depleted through depolarization mechanisms such as, for example, ionization from the electron beam. A failure to replenish the polarized gas quickly enough will result in a lower polarization in the target chamber than is the case in the pumping chamber, a condition we refer to herein as a *polarization gradient*.

Until relatively recently, polarization gradients in two-chambered cells have been at most a few percent relative. Advances in SEOP, however, have made it possible to run polarized  $^3\text{He}$  targets at increasingly high luminosities. During SLAC E142, where luminosities were in the range of  $0.42 - 1.70 \times 10^{35} \text{ cm}^{-2}\text{s}^{-1}$ , the polarization gradients were on the order of 1%. During more recent experiments at JLab, however, typical luminosities were in the range  $0.6 - 1.0 \times 10^{36} \text{ cm}^{-2}\text{s}^{-1}$  and polarization gradients were in the range of 5–6%. For future experiments with luminosities in the range of  $10^{37} \text{ cm}^{-2}\text{s}^{-1}$ , polarization gradients well in excess of 10% are likely if no changes are made to the basic target cell design. Polarization gradients can also be difficult to quantify accurately, an issue that can lead to larger uncertainties in polarimetry.

The fact that polarized  $^3\text{He}$  targets are being run at increasingly high luminosities is due largely to advances in SEOP. One example is the use of hybrid mixtures of alkali metals (typically potassium and rubidium) instead of a single alkali metal (typically rubidium)[13, 14]. This technique, often known as alkali-hybrid SEOP, greatly improves the efficiency with which the  $^3\text{He}$  is polarized. Another important advance has followed from the availability of commercial spectrally-narrowed high-power diode laser arrays. These new lasers result in significantly higher optical pumping rates for a given

amount of light. Collectively, these advances have made it possible to significantly increase the rate at which the  $^3\text{He}$  is polarized. It has become possible to achieve higher polarizations even when using higher beam currents and thicker targets. Higher currents, however, make it necessary to replenish the polarized gas in the target chamber more quickly. If the advances in SEOP are to be fully exploited, it is essential that the designs of polarized  $^3\text{He}$  targets evolve.

We report here on a new design for polarized  $^3\text{He}$  target cells that are polarized using SEOP. While similar in many respects to the design illustrated in Fig. 1, and used in the aforementioned experiments, the design incorporates the ability to circulate the gas between the pumping chamber and the target chamber using convection instead of diffusion. As will be discussed below, the convection is achieved by maintaining a temperature differential between different parts of the target cell, and does not involve pumps or other moving parts. We have built a prototype to demonstrate the convection concept, and have shown that the velocity of the gas moving through the target chamber can be varied between 5–80 cm/min in a simple controllable manner. The advent of a means to circulate a polarized noble gas in a sealed vessel without the use of pumps has great potential for high-luminosity polarized  $^3\text{He}$  targets. The simplicity of the approach has advantages from the perspective of reliability, and fast transport of gas between the two chambers makes it possible to greatly increase the electron beam current without causing a polarization gradient. Convection-based target cells also open the possibility of physically separating the pumping chamber and the target chamber by much larger distances than was previously possible, something that offers a number of practical advantages.

## II. POLARIZATION DYNAMICS AND GRADIENTS IN TWO-CHAMBERED CELLS

### A. The Single-Chambered Cell

Before considering the formalism for target cells with two chambers, we begin by considering the simpler example of a single-chambered cell, where the equation describing the time evolution of the polarization is given by:

$$\dot{P}_{\text{He}} = \gamma_{\text{se}} P_A - (\gamma_{\text{se}} + \Gamma) P_{\text{He}}, \quad (1)$$

where  $P_{\text{He}}$  is the  $^3\text{He}$  polarization,  $P_A$  is the polarization of the alkali vapor,  $\gamma_{\text{se}}$  is the rate at which the  $^3\text{He}$  is polarized due to spin exchange, and  $\Gamma$  is the spin-relaxation rate of the  $^3\text{He}$  due to all other processes. The solution to Eqn.1 is given by

$$P_{\text{He}}(t) = P_0 e^{-(\gamma_{\text{se}} + \Gamma)t} + P_A \frac{\gamma_{\text{se}}}{\gamma_{\text{se}} + \Gamma} (1 - e^{-(\gamma_{\text{se}} + \Gamma)t}) \quad (2)$$

where  $P_0$  is the  $^3\text{He}$  polarization at  $t = 0$ . It has been shown by Babcock *et al.* that one of the components

of  $\Gamma$  is a relaxation rate that empirically appears to be proportional to  $\gamma_{se}$  [15]. One can accordingly write that  $\Gamma = \Gamma' + \gamma_{se}X$ , where  $X$  is a proportionality constant. We can thus write the saturation polarization associated with Eqn. 2 as

$$P_{\text{He}}(t = \infty) = P_A \frac{\gamma_{se}}{\gamma_{se}(1 + X) + \Gamma'} \quad , \quad (3)$$

where we note that the denominator of 3 is also the rate that characterizes the buildup of polarization in 2, rewritten in terms of  $\Gamma'$  and  $X$ . The existence of a relaxation mechanism proportional to  $\gamma_{se}$  is unfortunate, as it implies that, even with a 100% polarized alkali vapor, in the limit that  $\gamma_{se} \rightarrow \infty$ ,  $P_{\text{He}} \rightarrow 1/(1 + X)$ . While not well understood, the existence of this additional relaxation is now well established, and is important for understanding the overall polarization achieved.

It is straightforward to project the performance of a target at a range of beam currents if we know how it performed at a particular beam current  $I_0$  (true even if  $I_0 = 0$ ). Let us assume that we have data on polarization as a function of time while polarizing the target from an initial polarization of zero. A plot of data of this sort is something we often refer to as a “spin-up curve”. We accordingly define the quantity  $\gamma_{su}^0$  that characterizes the rate at which the polarization increases during a spin-up:

$$\gamma_{su}^0 \equiv \gamma_{se}(1 + X) + \Gamma'(I_0) \quad . \quad (4)$$

Let us further define  $P_{\text{He}}^\infty(I_0)$  as the equilibrium polarization associated with that spin-up. Using Eqns. 3 and 4, we find

$$P_{\text{He}}^\infty(I_0) = P_A \gamma_{se} / \gamma_{su}^0 \quad . \quad (5)$$

Solving Eqn. 4 for  $\gamma_{se}(1 + X)$  and Eqn. 5 for  $P_A \gamma_{se}$  and substituting into Eqn. 3, we arrive at

$$P_{\text{He}}^\infty(I) = \frac{P_{\text{He}}^\infty(I_0) \gamma_{su}^0}{\gamma_{su}^0 - \Gamma'(I_0) + \Gamma'(I)} \quad . \quad (6)$$

The quantities  $P_{\text{He}}^\infty(I_0)$  and  $\gamma_{su}^0$  can be determined by fitting data from a spin up, and the quantity  $\Gamma'(I) = \Gamma_{wall}^{cold} + \Gamma_{dipole} + \Gamma_{beam}$ , where the three terms are spin-relaxation rates due to wall collisions (at room temperature), dipole interactions due to  ${}^3\text{He}$ - ${}^3\text{He}$  collisions, and ionization of the electron beam respectively. The sum of the first two terms are close to the target’s room-temperature spin-relaxation rate in the absence of beam. A small (calculated) correction can be applied to  $\Gamma_{dipole}$  to account for differences in the densities in the pumping and target chambers during running conditions. The contribution  $\Gamma_{beam}$  is easily computed [16, 17], and comparison with experiment has shown good agreement at a level of roughly 10% or better [18]. We can thus use Eqn. 6 to project the performance of a target at arbitrary beam current.

In Fig. 2, we use Eqn. 6 to project the polarization of two targets (each used in one of the aforementioned

experiments) as function of beam current. For the time being, we largely ignore the fact that both of these targets had two chambers, and return to this issue in the next subsection. The data points shown with closed circles represent measured polarizations at the indicated beam currents in the target chamber of each cell. The open points represent the polarization averaged over the entire cell, and is the quantity we use for  $P_{\text{He}}^\infty(I_0)$ . The cell “Minnehaha” was used during SLAC E142 [1] and was run at beam currents up to  $3.3 \mu\text{A}$ . The cell “Edna” was used during JLab E02-013 (GEN) [2] and was run at  $8 \mu\text{A}$ . The time constant  $\gamma_{su}^0$ , during running conditions, was in the approximate range of 15–20 hrs for Minnehaha, and 5–6 hrs for Edna.

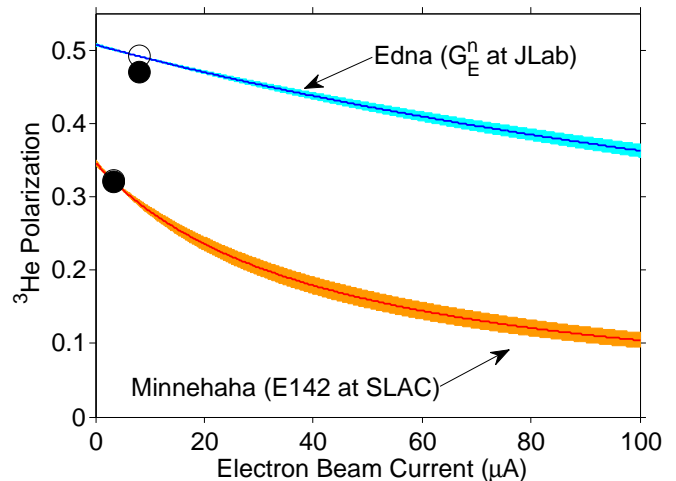


FIG. 2: Shown is the projected  ${}^3\text{He}$  polarization (averaged over the cell) as a function of beam current, calculated using Eqn. 6, for two targets, “Minnehaha” (used during SLAC E142) and “Edna” (used during JLab E02-013 (GEN)). The closed circles show the polarization measured in the target chamber of each cell during their respective experiments, and the open points indicate the corresponding cell-averaged polarizations. The inputs used for Eqn. 6 are discussed in the text, and the width of each band corresponds to the uncertainty we have assigned to the parameter  $\gamma_{su}$ .

The two targets included in Fig. 2 illustrate how improvements in SEOP make it possible to run polarized  ${}^3\text{He}$  targets at substantially higher luminosities than was previously possible. The shorter time constants associated with Edna were due to the use of alkali-hybrid SEOP, the first time this technology was used in the context of electron scattering. The rapid and more efficient spin exchange also made it possible to polarize a larger volume of gas, around 2.8 liters for Edna, in contrast to about 1.3 liters for Minnehaha. Edna also had a substantially higher polarization than Minnehaha, and this polarization is far more robust in the presence of higher beam currents. Not explicitly shown in Fig. 2 is that Edna had a higher operating density and a longer target length. The greater efficiency with which  ${}^3\text{He}$  nuclei can be polarized using alkali-hybrid SEOP greatly expands the target performance that is achievable.

## B. Time evolution in a double-chambered cell

For a full description of a double-chambered cell, the polarization build up must be described by the coupled differential equations first described in Ref. [12]:

$$\dot{P}_{\text{pc}} = \gamma_{\text{se}}(P_{\text{A}} - P_{\text{pc}}) - \Gamma_{\text{pc}}P_{\text{pc}} - d_{\text{pc}}(P_{\text{pc}} - P_{\text{tc}}) \quad (7)$$

$$\dot{P}_{\text{tc}} = -\Gamma_{\text{tc}}P_{\text{tc}} + d_{\text{tc}}(P_{\text{pc}} - P_{\text{tc}}) \quad (8)$$

where  $P_{\text{pc}}$  ( $P_{\text{tc}}$ ) is the  $^3\text{He}$  polarization in the pumping (target) chamber,  $\gamma_{\text{se}}$  is the spin-exchange rate in the pumping chamber, and  $\Gamma_{\text{pc}}$  and  $\Gamma_{\text{tc}}$  are the  $^3\text{He}$  spin-relaxation rates due to all other processes in the pumping and target chambers respectively. The transfer rate  $d_{\text{tc}}$  ( $d_{\text{pc}}$ ) is the probability per unit time per nucleus that a nucleus will exit the target (pumping) chamber and enter the pumping (target) chamber. We note that we do not include the transfer tube as a separate volume in the above discussion. The transfer rates are related by

$$f_{\text{pc}}d_{\text{pc}} = f_{\text{tc}}d_{\text{tc}} \quad (9)$$

where  $f_{\text{pc}}$  ( $f_{\text{tc}}$ ) is the fraction of atoms in the pumping (target) chamber, and  $f_{\text{pc}} + f_{\text{tc}} = 1$ . For the dynamic studies reported in Ref. [12], the authors were able to neglect terms involving  $\gamma_{\text{se}}$  and  $\Gamma$  relative to terms involving  $d_{\text{pc}}$  and  $d_{\text{tc}}$ . For the discussion here, however, we must retain these terms, and find that the solutions to Eqns. 7 and 8 have the following form (see Appendix A and Ref [19]):

$$P_{\text{pc}}(t) = C_{\text{pc}}e^{-\Gamma_{\text{f}}t} + (P_{\text{pc}}^0 - P_{\text{pc}}^\infty - C_{\text{pc}})e^{-\Gamma_{\text{s}}t} + P_{\text{pc}}^\infty \quad (10)$$

$$P_{\text{tc}}(t) = C_{\text{tc}}e^{-\Gamma_{\text{f}}t} + (P_{\text{tc}}^0 - P_{\text{tc}}^\infty - C_{\text{tc}})e^{-\Gamma_{\text{s}}t} + P_{\text{tc}}^\infty \quad (11)$$

where  $P_{\text{pc}}^0$  and  $P_{\text{tc}}^0$  are the initial polarizations in the pumping and target chambers respectively,

$$P_{\text{pc}}^\infty = \frac{\gamma_{\text{se}} f_{\text{pc}} P_{\text{A}}}{\gamma_{\text{se}} f_{\text{pc}} + \Gamma_{\text{pc}} f_{\text{pc}} + \Gamma_{\text{tc}} f_{\text{tc}} (1 + \frac{\Gamma_{\text{tc}}}{d_{\text{tc}}})^{-1}} \quad , \quad (12)$$

and

$$P_{\text{tc}}^\infty = P_{\text{pc}}^\infty \frac{1}{1 + \frac{\Gamma_{\text{tc}}}{d_{\text{tc}}}} \quad . \quad (13)$$

We have chosen to write Eqn. 12 in the form shown to emphasize that

$$\lim_{(\Gamma_{\text{tc}}/d_{\text{tc}}) \rightarrow 0} P_{\text{tc}}^\infty = \lim_{(\Gamma_{\text{tc}}/d_{\text{tc}}) \rightarrow 0} P_{\text{pc}}^\infty = \frac{P_{\text{A}} \langle \gamma_{\text{se}} \rangle}{\langle \gamma_{\text{se}} \rangle + \langle \Gamma \rangle} \quad (14)$$

where  $\langle \gamma_{\text{se}} \rangle$  is the spin-exchange rate averaged throughout the double-chambered cell ( $\langle \gamma_{\text{se}} \rangle = f_{\text{pc}}\gamma_{\text{se}}$ , since the spin-exchange rate is  $\gamma_{\text{se}}$  in the pumping chamber and is zero in the target chamber), and  $\langle \Gamma \rangle = f_{\text{pc}}\Gamma_{\text{pc}} + f_{\text{tc}}\Gamma_{\text{tc}}$  is the spin-relaxation rate averaged throughout the cell. Eqn. 14 has the same form as the saturation polarization

of Eqn. 2, as we would expect in the limit of infinitely fast transfer.

While the complete forms for  $C_{\text{pc}}$  and  $C_{\text{tc}}$  are given in Appendix A, we consider two particular cases. In the fast-transfer limit, the quantities  $C_{\text{pc}}$  and  $C_{\text{tc}}$  are given by

$$C_{\text{pc}} = f_{\text{tc}}(P_{\text{pc}}^0 - P_{\text{tc}}^0) \quad , \quad (15)$$

and

$$C_{\text{tc}} = f_{\text{pc}}(P_{\text{tc}}^0 - P_{\text{pc}}^0) \quad . \quad (16)$$

For the case in which  $P_{\text{pc}}^0 = P_{\text{tc}}^0 = 0$ , the quantities  $C_{\text{pc}}$  and  $C_{\text{tc}}$  are given by

$$C_{\text{pc}} = \frac{\Gamma_{\text{s}} P_{\text{pc}}^\infty - \gamma_{\text{se}} P_{\text{A}}}{\Gamma_{\text{f}} - \Gamma_{\text{s}}} \quad (17)$$

and

$$C_{\text{tc}} = \frac{\Gamma_{\text{s}} P_{\text{pc}}^\infty}{\Gamma_{\text{f}} - \Gamma_{\text{s}}} \quad . \quad (18)$$

The constants  $\Gamma_{\text{s}}$  and  $\Gamma_{\text{f}}$  represent slow and fast rates respectively that govern the time evolution of the polarization. It is useful to write  $\Gamma_{\text{s}}$  in the form

$$\Gamma_{\text{s}} = \langle \gamma_{\text{se}} \rangle + \langle \Gamma \rangle - \delta\Gamma \quad (19)$$

where the quantity  $\delta\Gamma$  is generally small and goes to zero in the limit of infinitely fast transfer between the two chambers. We can see that the limiting form of  $\Gamma_{\text{s}}$  has the same form as the time constant that appears in Eqn. 3 ( $\gamma_{\text{se}} + \Gamma$ ). In Appendix A we show that

$$\delta\Gamma = \frac{d_{\text{pc}} + d_{\text{tc}}}{2} \left[ \sqrt{1 - 2u\delta f + u^2} - 1 + u\delta f \right] \quad (20)$$

where  $\delta f = f_{\text{pc}} - f_{\text{tc}}$  and

$$u = \frac{\gamma_{\text{se}} + \Gamma_{\text{pc}} - \Gamma_{\text{tc}}}{d_{\text{pc}} + d_{\text{tc}}} \quad . \quad (21)$$

For most of the situations we would normally consider, the quantity  $u$  is fairly small. This is due to two things. First, the spin-exchange rate  $\gamma_{\text{se}}$  is typically slow compared to the sum of the two transfer rates  $d_{\text{pc}}$  and  $d_{\text{tc}}$ , and second, both  $\Gamma_{\text{pc}}$  and  $\Gamma_{\text{tc}}$  must be relatively small compared to  $\gamma_{\text{se}}$ , or the polarization of the target would not be high. Of the two relaxation rates  $\Gamma_{\text{pc}}$  and  $\Gamma_{\text{tc}}$ , the latter (which enters with a minus sign) is likely to be the larger (particularly if beam depolarization is present) which also helps ensure that the numerator is small compared to the denominator. It is thus reasonable to expand  $\delta\Gamma$  in a Taylor series in  $u$ :

$$\delta\Gamma \approx f_{\text{pc}}f_{\text{tc}}(d_{\text{pc}} + d_{\text{tc}})u^2 \quad . \quad (22)$$

Lastly, we consider  $\Gamma_{\text{f}}$  which can be written as

$$\Gamma_{\text{f}} = (d_{\text{pc}} + d_{\text{tc}}) + (\gamma_{\text{se}} - \langle \gamma_{\text{se}} \rangle) + (\Gamma_{\text{pc}} + \Gamma_{\text{tc}} - \langle \Gamma \rangle) + \delta\Gamma \quad . \quad (23)$$

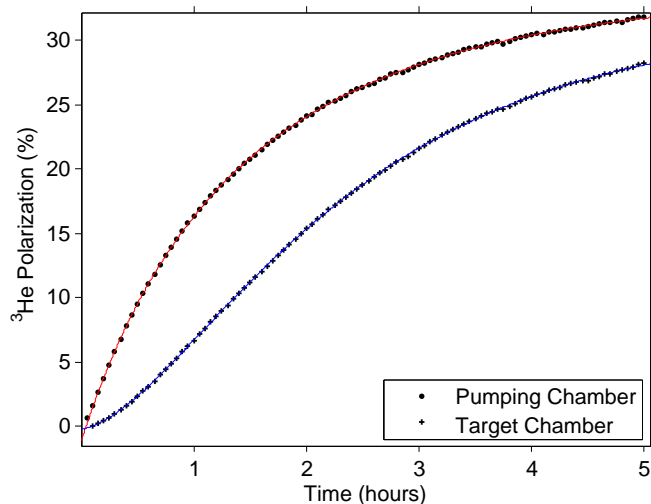


FIG. 3: The  $^3\text{He}$  polarization is shown as a function of time for both the pumping chamber (upper curve) and target chamber (lower curve) of the target cell “Brady”. In this case the lasers were turned on immediately before data taking to ensure an initial polarization of zero. Also shown are fits to Eqns. 10 and 11. We refer to curves of this sort as spinup curves. AFP measurements were made rapidly (every 3 minutes).

In the fast-transfer limit,  $\Gamma_f \rightarrow \infty$ ; under these conditions, Eqns. 10 and 11 reduce to the form of Eqn. 2.

Data illustrating the time evolution of polarization (what we referred to earlier as a spin-up) are shown in Fig. 3 for both the pumping and target chambers of a double-chambered cell we refer to herein as “Brady”. The polarization was measured every three minutes using the NMR technique of adiabatic fast passage (AFP) [20]. We note that under normal operating conditions, NMR measurements would only be made once every few hours, in part because each measurement results in a small loss ( $< 1\%$ ) of polarization. The frequent measurements shown in Fig. 3 strongly limit the saturation polarization because of accumulating losses. Also shown in Fig. 1, but obscured beneath the many data points, is a fit to the data using double-exponential functions of the form given in Eqns. 10 and 11. The fit clearly describes the data quite well.

Finally, we note that in the context of the types of cells that have been used in electron-scattering experiments (see Fig. 1), the mechanism behind the transfer rates  $d_{tc}$  and  $d_{pc}$  is overwhelmingly diffusion.

### C. Initial Polarization Evolution

Some of the parameters discussed earlier can be readily determined by studying spinup curves of the sort shown in Fig. 3. To extract values for the transfer rates  $d_{pc}$  and  $d_{tc}$ , it is particularly valuable to examine the spinup curves for the initial time period during which the polarization is growing. For small values of the time  $t$ , it is readily apparent from Fig. 3 that the nature of the time

evolution in the two chambers is quite different. Under the assumption that the time  $t < 1/\Gamma_f$  (in this case,  $1/\Gamma_f \approx 0.75\text{hrs}$ ), we can expand Eqns. 10 and 11 in a Taylor series. To second order, for the case of  $P_{pc}^0 = P_{tc}^0 = 0$ , this expansion simplifies to:

$$P_{pc}(t) = \gamma_{se}P_A t - \frac{1}{2}\gamma_{se}P_A(\gamma_{se} + \Gamma_{pc} + d_{pc})t^2 \quad (24)$$

$$P_{tc}(t) = \frac{1}{2}\gamma_{se}P_A d_{tc}t^2. \quad (25)$$

In Fig. 4, we show only the first 24 minutes of the data shown in Fig. 3. It can be seen that the initial shape of spinup curve appears to be linear in the pumping chamber and quadratic in the target chamber, in agreement with expectations from Eqns. 24 and 25.

Measurements of the early time behavior of the polarization buildup can provide valuable information that translates into a better understanding of the difference in polarization between the pumping and target chambers under operating conditions. The slope of the polarization buildup in the pumping chamber is proportional to the product  $P_A\gamma_{se}$ . Given appropriate diagnostics,  $P_A$  is reasonably straightforward to measure. For the data shown in Figs. 3 and 4,  $P_A = 99 \pm 3\%$ . Using this value and the slope of the polarization buildup in the pumping chamber, we find that  $\gamma_{se} = (0.25 \pm 0.025)\text{hrs}^{-1}$ . With this number in hand, we can fit the coefficient of the quadratic buildup of polarization in the target chamber, finding  $d_{tc} = (0.72 \pm 0.10)\text{hrs}^{-1}$ . As will be discussed in the next subsection, a value for  $d_{tc}$  can also be computed from first principles given the dimensions of the cell. The comparison of this value with that resulting from the fits described above provides insight into the degree to which we understand the diffusion processes taking place in our cells.

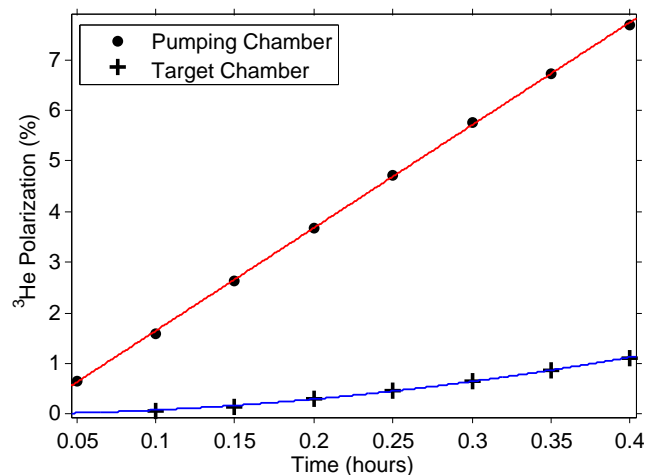


FIG. 4: Early time behavior of the Brady spinup shown in Fig. 3.

### D. Transfer Rates Under Diffusion

Using gas kinetic theory, the dimensions of the target cell, the density of  $^3\text{He}$  and other gases when the cell was filled, the operating temperatures of the pumping and target chambers and the assumption that the temperature gradient along the transfer tube is linear, it is possible to compute  $d_{pc}$  and  $d_{tc}$  from first principles. We begin similarly to the discussion in Ref. [12] with an equation describing the net polarization flux  $J_{tt}$  through the transfer tube:

$$J_{tt} = -n(z) D(z) \frac{dP(z)}{dz} \quad (26)$$

where  $n(z)$ ,  $D(z)$  and  $P(z)$  are the  $^3\text{He}$  number density, self-diffusion constant and polarization respectively, all shown as a function of position  $z$  along the transfer tube. As discussed by Romalis [21] and later by Zheng [22], using data on the self-diffusion constant of  $^4\text{He}$  by Kestin *et al.* [23], the self diffusion constant for  $^3\text{He}$  is well approximated by the expression

$$D(z) = D_0 \left( \frac{T(z)}{T_0} \right)^{m-1} \left( \frac{n_0}{n(z)} \right) \quad (27)$$

where  $D_0 = 2.789 \text{ cm}^2/\text{s}$ ,  $T_0 = 353.14 \text{ K}$ ,  $m = 1.705$  and  $n_0 = 0.7733 \text{ amg}$  ( $1 \text{ amg} = 2.687 \times 10^{19} \text{ cm}^{-3}$ ). The assumption of a linear temperature gradient along the transfer tube between the pumping and target chambers, as was assumed in Refs. [21, 22], allows us to express  $T(z)$  and hence  $n(z)$  explicitly. With this assumption, and substituting Eqn. 27 into Eqn. 26, we can solve for  $J_{tt}$  to find

$$J_{tt} = -(P_{pc} - P_{tc}) D_0 \frac{n_0 (2 - m) (T_{pc} - T_{tc})}{L_{tt} (T_0^{m-1}) (T_{pc}^{2-m} - T_{tc}^{2-m})}. \quad (28)$$

$J_{tt}$  is the total rate of polarization transfer per unit area, whereas we want the rate per atom. Multiplying by the transfer tube cross sectional area  $A_{tt}$ , dividing by the number of particles in each chamber, and finally dividing by  $(P_{pc} - P_{tc})$ , we have

$$d_{tc(pc)} = \frac{A_{tt} D_0}{V_{tc(pc)} L_{tt}} \frac{n_0 (2 - m) (T_{pc} - T_{tc})}{n_{tc(pc)} (T_0^{m-1}) (T_{pc}^{2-m} - T_{tc}^{2-m})}. \quad (29)$$

Of specific interest here is the value for  $d_{tc}$  implied by Eqn. 29 for the target cell Brady. For Brady,  $A_{tt} = 0.667 \text{ cm}^2$ ,  $L_{tt} = 9.07 \text{ cm}$ ,  $V_{tc} = 74.6 \text{ cm}^3$ , and  $n_{tc} = 11.5 \text{ amg}$ . Using temperatures that correspond to the tests illustrated in Figs. 3 and 4, we find  $d_{tc} = 0.72 \text{ hrs}^{-1}$ , a value that agrees fortuitously with the value found by fitting the polarization buildup curves.

### E. Polarization Gradients

An issue of considerable practical importance for polarized  $^3\text{He}$  targets is the polarization gradient between

the pumping and target chambers. Dividing both sides of Eqn. 13 by  $P_{pc}^\infty$ , we find

$$\frac{P_{tc}^\infty}{P_{pc}^\infty} = \frac{1}{1 + \Gamma_{tc}/d_{tc}}. \quad (30)$$

It is also useful to define the quantity  $\Delta$ , the amount by which the polarization in the target chamber is lower than that of the pumping chamber. Here we express this difference as a fraction of the pumping chamber polarization:

$$\Delta \equiv \frac{P_{pc}^\infty - P_{tc}^\infty}{P_{pc}^\infty} = \frac{1}{1 + d_{tc}/\Gamma_{tc}} \quad (31)$$

We can see that  $\Delta$  approaches 0 for cells in which  $\Gamma_{tc}$  is quite slow and  $d_{tc}$  is quite fast. The fact that it is  $\Gamma_{tc}$  and not the cell-averaged relaxation rate  $\langle \Gamma \rangle$  that appears in this expression is quite important. When a target is subjected to high electron-beam currents, the overall cell-averaged relaxation rate  $\langle \Gamma \rangle$  may not be strongly affected even though the local relaxation rate in the target chamber  $\Gamma_{tc}$  is. As stated earlier, what is important is that the polarized gas in the target chamber is replenished at a rate that is much faster than the rate at which the gas is depolarized in the target chamber.

#### 1. Examples of polarization gradients

To best understand the increasing importance of polarization gradients, it is useful to consider the size of the effect for the two targets that were discussed in the context of Fig. 2. In Fig. 5 below, we use Eqn. 31 to plot  $\Delta$  as a function of beam current for both cells. For  $d_{tc}$ , we used Eqn. 29, together with the known geometry and fill densities of the respective cells, and typical operating temperatures. The determination of  $\Gamma_{tc}$ , the relaxation rate specific to the target chamber, is more problematic because it is never measured directly. In Fig. 5, a conservative estimate of this uncertainty is represented by the shaded bands. A discussion of how we constrain values for  $\Gamma_{tc}$  is discussed in the next subsection.

Several trends evident in Fig. 5 are important when considering the next generation of polarized  $^3\text{He}$  targets. Most importantly, for both targets shown,  $\Delta$  becomes undesirably large at higher beam currents. It can also be seen that both the magnitude and the uncertainty of the gradients are worse for Edna than they are for Minnehaha. The gradient  $\Delta$  is strictly a function cell geometry, density, the temperatures at which the cell is run, and  $\Gamma_{tc}$  (which is affected by the electron beam). As such,  $\Delta$  is not directly affected by the advancements in SEOP that were discussed earlier. There is, however, an indirect connection. Advances in SEOP have made it possible to build larger targets, with faster spin-exchange rates  $\gamma_{se}$ , while using similar or even lower levels of laser power. For example, a target with a large ballast volume of  $^3\text{He}$ , in the form of a large pumping chamber, will be

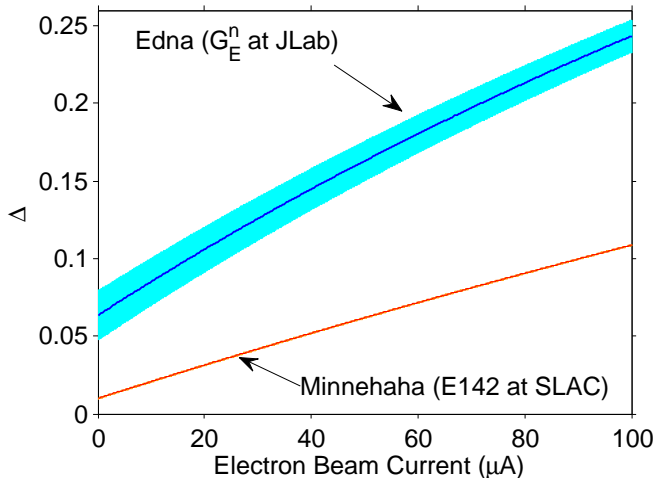


FIG. 5: Shown are the calculated polarization gradients (using Eqn. 31) as a function of electron beam current for two target cells. The width of the band is due to the uncertainty in the target chamber spin-relaxation rate,  $\Gamma_{tc}$ .

less susceptible to depolarization from the electron beam. For Edna, designed to run at currents up to  $15 \mu\text{A}$  (but actually run at  $8 \mu\text{A}$ ), the ratio of the pumping chamber volume  $V_{pc}$  to the target chamber volume  $V_{tc}$  was 3.6:1. For Minnehaha, the same ratio was 0.79:1. As will be seen in the next section, the difference in  $V_{pc}/V_{tc}$  contributes to the uncertainty in  $\Delta$  (represented by the band in Fig. 5). The larger pumping chamber also necessitates a larger distance between the pumping chamber and the target chamber, something that contributes to the magnitude of  $\Delta$ . In the future, it will become increasingly important to increase the distance between the pumping chamber and the target chamber even further to facilitate radiation shielding. Also contributing to the larger magnitude of  $\Delta$  for Edna is the fact that Edna had a higher operating density in the target chamber. While it is possible to compensate for these effects by increasing somewhat the diameter of the transfer tube, the message is clear. Diffusion becomes a limiting factor in performance as polarized  $^3\text{He}$  targets are operated at increasingly high luminosities.

## 2. Constraining $\Gamma_{tc}$

A limiting factor in quantifying polarization gradients is uncertainty in  $\Gamma_{tc}$ . The quantity that is most straightforward to measure experimentally is a target's room-temperature cell-averaged spin-relaxation rate,  $\langle\Gamma\rangle$ , which is typically due to three primary contributions:

$$\langle\Gamma\rangle = \Gamma^w + \Gamma^d + \Gamma^b \quad (32)$$

where  $\Gamma^w$  is the spin relaxation rate due to wall collisions,  $\Gamma^d$  is spin relaxation due to dipolar interactions during  $^3\text{He} - ^3\text{He}$  collisions and  $\Gamma^b$  is the spin relaxation due to the electron beam, which can be taken to be zero if the cell's spin-relaxation rate is measured in the absence of an electron beam. The wall relaxation rate will be the sum of the wall relaxation rates in the target and pumping chambers respectively, weighted by the fraction of  $^3\text{He}$  atoms that are in each chamber:

$$\Gamma^w = f_{tc}\Gamma_{tc}^w + f_{pc}\Gamma_{pc}^w \quad (33)$$

For the purposes of this discussion, it is convenient to introduce a parameter  $R$ , representing the ratio of  $\Gamma_{tc}^w$  to  $\Gamma_{pc}^w$ , so that

$$\Gamma_{tc}^w = R\Gamma_{pc}^w \quad (34)$$

From Eqns. 32–34, taking  $\Gamma^b = 0$ , we find an expression for  $\Gamma_{tc}^w$ :

$$\Gamma_{tc}^w = \frac{R(\langle\Gamma\rangle - \Gamma^d)}{f_{tc}R + f_{pc}} \quad (35)$$

Unfortunately, we have no direct measurement of  $R$ . One plausible assumption is that  $\Gamma_{tc}^w = \Gamma_{pc}^w$ , in which case  $R = 1$ , and Eqn. 35 implies that  $\Gamma_{tc}^w = \Gamma_{pc}^w = \langle\Gamma\rangle - \Gamma^d$ . There is considerable discussion in the literature on SEOP, however, that suggests that, all other things being equal, wall relaxation should be proportional to the surface-to-volume ratio of the vessel containing the gas. If this is assumed, we would expect  $R$  to be the ratio of the surface-to-volume ratios of the pumping and target chambers respectively, a quantity we will refer to here as  $R_{max}$ . In Fig. 5, the solid lines correspond to the assumption that  $R = (1 + R_{max})/2$ . The two bands represent the range of values for  $\Delta$  under the conservative assumption that  $1 < R < R_{max}$ .

In addition to limiting target performance, polarization gradients can in practice introduce systematic uncertainties into polarimetry. One of the best techniques for determining the absolute polarization of  $^3\text{He}$  is the method of measuring shifts in the electron paramagnetic resonance frequencies of the alkali-metal atoms due to the effective magnetic field caused by the polarized  $^3\text{He}$  [24]. This can only be performed in the pumping chamber, despite the fact that the quantity of interest in an electron scattering experiment is the polarization in the target chamber. Thus, it is often the case that NMR measurements are made directly on the target chamber, but are calibrated against frequency shift measurements in the pumping chamber. When this is done, the calibration requires a knowledge of  $\Delta$ . In the case of the cell Edna, for instance, referring to Fig. 5 with zero beam current, we show  $\Delta = 6.32 \pm 1.58\%$ , where the quoted error covers the full range of  $1 < R < R_{max}$ . While an additional (relative) error in polarimetry of  $\pm 1.64\%$  is not catastrophic, it would certainly be nice to avoid.

### 3. Implications of a single transfer tube

Two points emerge regarding polarization gradients: 1) they severely limit target polarization at high beam currents, and 2) they are somewhat uncertain in their size, which in some circumstances, results in systematic uncertainties in experiments. If we want to make polarization gradients smaller while retaining the basic cell design illustrated in Fig. 1, by examining Eqn. 29, we see that there are two things that can be done. We can make the cross sectional area of the transfer tube larger, and we can make the length of the transfer tube shorter. We can certainly ameliorate some of the problems in this fashion, perhaps extending the utility of the single-transfer tube approach to higher currents.

There is an issue, however, that has not yet been discussed. Glass target cells filled with  $^3\text{He}$  have a tendency to rupture once they have been exposed to an electron beam for an extended period of time. Ironically, the rupture often occurs not in the target chamber, through which the electron beam passes, but instead in the pumping chamber. A reasonable explanation is that radiation damage occurs over time, and in the relatively large pumping chamber, where the stresses are greatest, a rupture is more likely to occur. If radiation damage is indeed the cause of the ruptures, there is every reason to expect the glass cells used in polarized  $^3\text{He}$  targets to rupture more quickly when exposed to higher beam currents. It would thus be desirable to physically locate the pumping chamber further from the beam to lessen the exposure to radiation. This is directly opposed to what is needed, however, to minimize polarization gradients. As we will show below, a cell with two transfer tubes, in which convection causes the mixing of the gas, addresses all of these issues. The polarization gradients can be made arbitrarily small while simultaneously moving the pumping chamber as far away from the beam as is desired.

## III. CONVECTION DRIVEN CELLS

We describe next a variant of the target cell geometry that is depicted in Figure 1. There are still two chambers, a pumping chamber and a target chamber, but the two chambers are connected by two transfer tubes instead of one. With this design, it is possible to induce convection, thus causing rapid transfer of gas between the two chambers. Furthermore, all that is required to induce convection is to maintain a temperature differential between the vertical segments of the two transfer tubes. By controlling the temperature differential, the speed of the convection can be adjusted. With rapid mixing of gas between the two chambers, the aforementioned polarization gradients can be made negligible, even if the distance between the pumping and target chambers is substantially increased.

## A. Experimental Setup

To demonstrate the feasibility of convection-driven polarized  $^3\text{He}$  target cells, we have constructed a prototype with the geometry and dimensions illustrated in Fig. 6. The cell was constructed entirely out of aluminosilicate glass (GE 180), and was sealed after being filled with 7.2  $\mu\text{mol}$  of  $^3\text{He}$  and a 0.11  $\mu\text{mol}$  of  $\text{N}_2$ . The pumping chamber also contained several tens of milligrams of a hybrid mixture of potassium and rubidium metal.

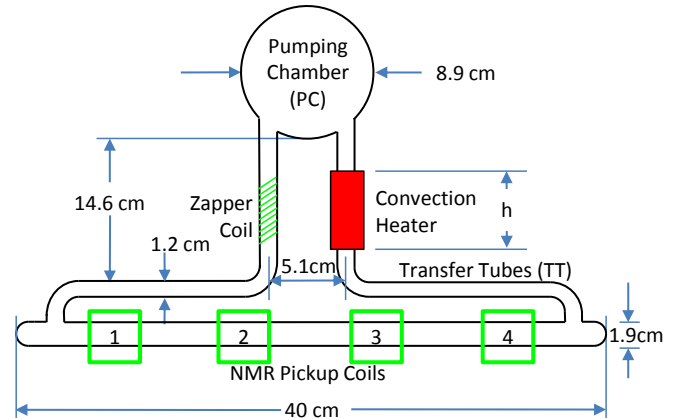


FIG. 6: Prototype convection-based target cell. The pumping chamber is placed inside of an optical pumping oven. The right transfer tube is heated while the left transfer tube is kept at room temperature. The two transfer tubes have different densities which creates a counter-clockwise convection current in the cell. The zapper coil is used to depolarize a slug of gas. This slug is then monitored as it travels through the pickup coils on the target chamber. We note that a small horizontal portion of the transfer tube was also heated, but for clarity is not shown, since it did not contribute to driving convection.

The  $^3\text{He}$  gas in the new prototype was polarized in the same manner as in our other target cells. The pumping chamber was surrounded by a forced-hot-air oven, constructed largely out of ceramic and glass. While polarizing the  $^3\text{He}$ , the oven was maintained at temperatures that were typically between 200 – 235°C, resulting in a vapor pressure of alkali-metal atoms corresponding to a number density on the order of  $10^{15}\text{cm}^{-3}$ . The rubidium atoms were optically pumped using laser light from high-power diode-laser arrays with a wavelength of 795 nm, and as described in refs. [13] and [14], quickly shared their polarization with the potassium atoms that were also present. Subsequent spin-exchange collisions with the  $^3\text{He}$  atoms resulted in the buildup of substantial nuclear polarization.

The temperature differential used to induce convection was maintained by using a second forced-hot-air “convection heater”, installed on one of the transfer tubes as illustrated on Fig. 6 (we note that, in reality, the convection heater also covered much of the horizontal portion of the transfer tube, but that this portion contributed negligibly to the speed of the convection). With a portion

of one of the transfer tubes at an elevated temperature, the gas contained therein had a lower density than the corresponding gas in the other transfer tube, and thus experienced a small buoyant force which induced convection. By controlling the temperature of the convection heater, the gas flow could be controlled in a stable and reproducible fashion.

The flow of the gas was monitored using an NMR tagging technique. A “slug” of gas within a small section of one of the transfer tubes was depolarized by subjecting it to a pulse of RF tuned to the Larmor frequency of the  $^3\text{He}$  nuclei. The RF was delivered using a small coil (labeled in Fig. 6 as the “Zapper coil”) wrapped directly around one of the transfer tubes. NMR signals were then detected at each of four locations along the target chamber using four “pickup coils” (see Fig. 6) comprised of small coils of wire wrapped around the target chamber. The movement of the slug of gas could then be tracked by monitoring NMR signals from each of the four coils. Signals from all four coils were obtained once every two seconds using the NMR technique of adiabatic fast passage (AFP)[20]. Representative examples of such signals are plotted in Fig. 7 as a function of time. Time zero in this plot corresponds to the moment when a slug of gas was tagged.

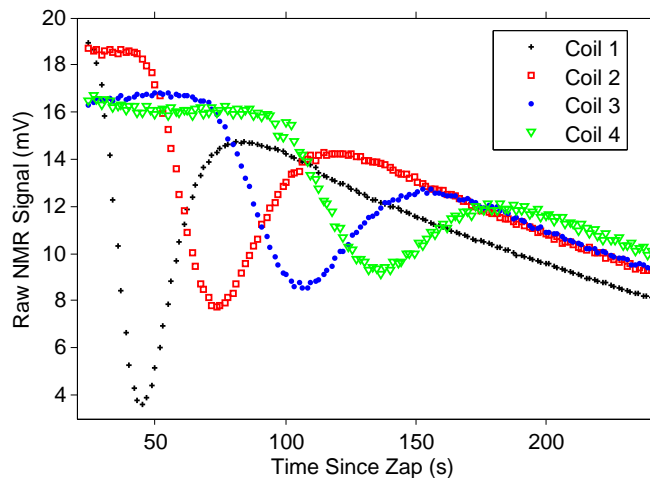


FIG. 7: Data used to visualize gas flow are shown in which the NMR signal from four pickup coils are plotted versus time. The oven temperature was  $215^\circ\text{C}$ , and the transfer tubes were  $24^\circ\text{C}$  and  $50^\circ\text{C}$  respectively. The data indicate a gas flow velocity of  $20\text{ cm/min}$  in the target chamber.

It is readily apparent from Fig. 7 that a transient dip occurs in each of the signals from the four pickup coils. This dip corresponds to the passage of the depolarized slug of gas, and it can be seen that the transient occurs at successively later times for each of coils 1–4. Given the known positions of the regularly spaced pickup coils, the difference in time between the transients associated with each of the four pickup coils provides a measure of the speed with which the tagged slug of gas was moving.

The measurement illustrated in Fig. 7 corresponds to a target-chamber gas velocity of  $20\text{ cm/minute}$ .

Also apparent from Fig. 7 is the fact that each successive dip becomes wider and more shallow. This is due in part to the fact that the gas flow within the cell is characterized by the classic parabolic Hagen-Poiseuille velocity distribution. That is, the velocity as a function of the distance  $r$  from the middle of the tube has the functional form  $v(r) = v_{max}(1 - r^2/R^2)$ . Hence, the slug of gas, which is initially fairly localized to the region around the “zapper coil”, becomes increasingly spread out as it moves through the target chamber. Additional spreading also occurs because of diffusion. We note also that the NMR signal decreases as a function of time. This is due largely to polarization losses that occur with each AFP measurement. While the loss from each individual measurement is quite small (on the order of 1%), the accumulation of many such losses is quite substantial. We note that in the normal operation of a polarized  $^3\text{He}$  target measurements are typically made not every two seconds, but rather every two to four hours.

## B. Temperature dependence of the gas velocity

Hagen-Poiseuille flow occurs whenever a pressure differential between two ends of a pipe causes the laminar flow of a viscous gas or fluid [25, 26]. In equilibrium, the driving force from the pressure differential  $F_{\text{driving}}$  must be equal to the retarding force  $F_{\text{retarding}}$  from the viscosity:

$$F_{\text{driving}} = F_{\text{retarding}} \quad (36)$$

For the case of a pipe that is circular in cross section, Eqn. 36 must be satisfied for each annular ring of fluid of thickness  $dr$ , a condition which leads to the equation

$$\Delta P 2\pi r dr = -2\pi\eta l \frac{d}{dr} \left( r \frac{dv}{dr} \right) dr \quad (37)$$

where  $\Delta P$  is the pressure differential,  $\eta$  is the viscosity of the fluid and  $l$  is the length of the pipe. Imposing the boundary condition that the velocity of flow must go to zero at the perimeter of the pipe, the solution to this differential equation is

$$v(r) = \frac{1}{4} \frac{\Delta P (r^2 - R^2)}{\eta l} \quad (38)$$

where  $R$  is the radius of the pipe. It is the velocity distribution given by Eqn. 38 that is often referred to as Hagen-Poiseuille Flow.

In the case of our convection cell the driving force is due to the small buoyancy force that results from maintaining a verticle portion of one transfer tube at a higher temperature than the corresponding section of the other transfer tube:

$$F_{\text{buoyancy}} = \Delta\rho V_t g \quad (39)$$

where  $V_t$  is the volume of the verticle portion of the transfer tube that is being heated,  $\Delta\rho$  is the difference between the average densities of the heated and unheated portions of the transfer tubes, and  $g$  is the acceleration due to gravity. We can express  $\Delta\rho$  as follows:

$$\Delta\rho = \rho T_C \left( \frac{1}{T_C} - \frac{1}{T_H} \right) \quad (40)$$

where  $\rho$  is the density of the gas in those portions of the cell that are not heated,  $T_C$  is the temperature of those portions of the cell that are not heated, and  $T_H$  is the temperature of the portion of the transfer tube that is being heated (both temperatures are in Kelvin). For the case being discussed here, the pressure differential that appears in the left-hand side of Eqn. 37 is thus given by

$$\Delta P = F_{\text{buoyancy}}/A_t = \Delta\rho h g, \quad (41)$$

where  $A_t$  is the cross sectional area of the transfer tube, and  $h$  is the length of the portion of the transfer tube that is heated.

If our convection cell could be treated as a long straight tube, we could simply substitute Eqns. 40 and 41 into Eqn. 38 to obtain an expression for the velocity. Our convection cells are more complicated, however which complicates the expression that appears on the right-hand side of Eqn. 37. There are multiple sections of tubing, each with its own radius, as well as bends etc. The velocity of the gas will be different in each section, and even the viscosity will be different depending on the temperature. Luckily, however, as will be shown in Appendix B, the continuity equation ensures that the velocity in each section is related in a simple linear fashion to the velocity in the other sections, so it is still possible to solve Eqn. 37 exactly. In essence, the quantity  $\eta l$  that appears on the right-hand side of Eqn. 37 must be replaced by a single quantity  $k_{\eta\mathcal{L}}$ , which still has the dimensions of viscosity times length, but incorporates the full complexity of the cell. The solution can accordingly be written in the form

$$v(r, T_H) = \frac{(r^2 - R^2)}{4k_{\eta\mathcal{L}}} \rho h g T_C \left( \frac{1}{T_C} - \frac{1}{T_H} \right), \quad (42)$$

where  $r$  is the radial coordinate in the target chamber, and  $R$  is the radius of the target chamber. The temperature dependence of  $v$  is largely dominated by the factor  $(\frac{1}{T_C} - \frac{1}{T_H})$ . The quantity  $k_{\eta\mathcal{L}}$ , however, is also dependent on temperature, although for the range of values of  $T_H$  that we consider, the temperature dependence of  $k_{\eta\mathcal{L}}$  on  $T_H$  is relatively weak.

It is important to understand the relationship between the observed velocity of the gas,  $v^{obs}$ , as indicated by data of the sort shown in Fig. 7, and the velocity distribution given by Eqn. 42. The natural way to compute  $v^{obs}$  is by taking the physical separation of adjacent pickup coils, and dividing by the separation in time between the minima of the corresponding transients. If we consider the limit in which the distance between the zapper coil and

the pickup coils is long compared to the length of the zapper coil itself, it is straightforward to show that, to a good approximation, the above method of computing  $v^{obs}$  corresponds to the maximum value of the velocity given by Eqn. 42,  $v^{max}$ , which results from setting  $r = 0$ . To a good approximation, we can express  $v^{max}$  in the simplified form

$$v^{max} = \frac{\mathcal{A}}{1 + \beta_1 \Delta T} \left( \frac{1}{T_C} - \frac{1}{T_H} \right), \quad (43)$$

where all quantities not dependent on  $T_H$  have been absorbed into the constant  $\mathcal{A}$ , and the temperature dependence of  $k_{\eta\mathcal{L}}$  is accounted for by the factor  $1 + \beta_1 \Delta T$ , where  $\Delta T = T_H - T_C$ . For the conditions we have considered,  $\beta_1$  is on the order of  $10^{-3}/^\circ\text{C}$ .

In Fig. 8 we have plotted  $v^{obs}$  as a function of  $T_H$  for a range of temperatures. For each point, the velocity was computed using data such as those shown in Fig. 7. We also show in Fig. 8 with a solid black line a fit of the data to a function of the form of Eqn. 43. The quality of the fit is clearly quite good, and yields the values  $\mathcal{A} = 7.47(22) \times 10^4 \text{K}\cdot\text{cm}/\text{min}$ ,  $T_{cold} = 24.3(8)$ , and  $\beta_1 = -0.2(2) \times 10^{-3}/^\circ\text{C}$ . For comparison, using our best knowledge of the cell geometry and densities, with  $T_{cold} = 24.5^\circ\text{C}$ , we compute  $\mathcal{A} = 9.14 \times 10^4 \text{K}\cdot\text{cm}/\text{min}$  and  $\beta_1 = 1.03 \times 10^{-3}/^\circ\text{C}$ . Given the uncertainties of some of the quantities with which we are working, particularly in describing the retarding forces associated with our relatively complicated cell geometry, this agreement is quite reasonable. More importantly, the agreement is more than sufficient to suggest that we have a reasonable quantitative understanding of the parameters influencing the convective flow from a practical perspective.

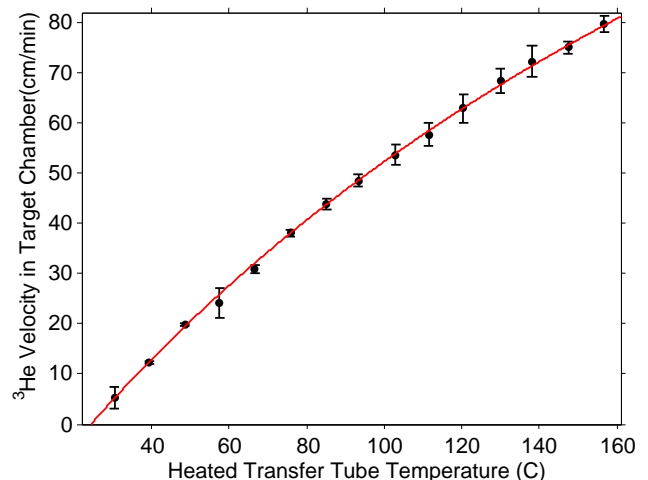


FIG. 8: The velocity of the gas in the target chamber is shown as a function of the temperature  $T$  of the heated transfer tube. The oven temperature was  $215^\circ\text{C}$  and the unheated transfer tube was at  $24^\circ\text{C}$ .

### C. Convection Transfer Rates and the Elimination of polarization gradients

Ultimately, the value of a convection-driven target cell is measured by the degree to which polarization gradients can be avoided between the pumping chamber and the target chamber. It is critical that, as gas is depolarized by an electron beam, freshly polarized gas is delivered from the pumping chamber sufficiently quickly. Ideally, one would like the ratio of the polarizations of the two chambers to be as close to unity as possible. Fortunately, when convection is used to transfer gas between chambers, the polarization gradient between chambers is suppressed. This is because the transfer rates can be quite high in the convection cell.

For the range of velocities measured in Fig. 8, we find values for  $d_{tc}$  in the range of 5 – 80  $\text{hrs}^{-1}$ . Even with relatively fast relaxation in the target chamber (for example, consider  $\Gamma_{tc} = 1/10\text{hrs}^{-1}$ ), the polarization gradient (Eqn. 31) will be very small in the presence of such fast transfer rates ( $\Delta \leq 0.02$ , or  $P_{tc}/P_{pc} \geq 0.98$ ).

In Fig. 3, the  $^3\text{He}$  polarization in both chambers of a traditional target cell is plotted as a function of time. The ratio of target chamber to pumping chamber polarization for this plot begins at zero, and gradually climbs to a value less than unity, reflecting a substantial polarization gradient. In Fig. 9, we plot this ratio for a convection-driven cell for three different operating conditions. In all cases, the temperature of the oven was held at 215 °C. The three curves correspond to different temperatures  $T_H$  of the heated transfer tube. For the data shown with the open squares, the transfer-tube set temperature was 24 °C, the same as the other (unheated) transfer tube. This case corresponds to no driven convection. For the data shown with the filled triangles, the set temperature was 50 °C, and for the data shown with the filled circles, the set temperature was 100 °C. These last two conditions corresponded to target-chamber gas velocities of approximately 19.9 cm/min and 48.5 cm/min. In both of these cases, the ratio of the polarizations of the target chamber and the pumping chamber quickly reached a value close to unity. It is notable that there is very little difference between these last two curves despite substantially different gas velocities. In short, as soon as convection rather than diffusion is responsible for the gas transfer between the two chambers, polarization is relatively uniform throughout the cell.

## IV. OUTLOOK FOR FUTURE TARGETS

The discussion in section IIA makes it clear that, apart from the issues associated with two-chambered target cells, it is becoming possible to run polarized  $^3\text{He}$  targets at increasingly high luminosities while still maintaining high polarization. The discussion of polarization gradients in section IIE, however, makes it clear that the current cell design, with one transfer tube, introduces

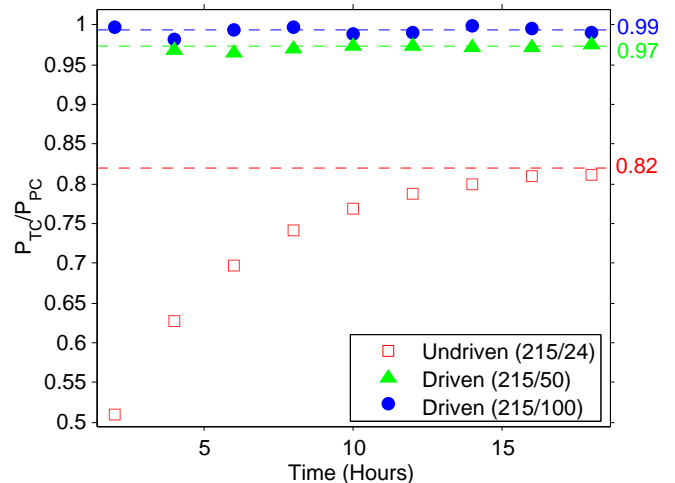


FIG. 9: The ratio of the polarizations of the target chamber and the pumping chamber,  $P_{tc}/P_{pc}$ , is shown versus time for 3 spinups corresponding to different convection velocities.

limitations. At the present time, these limitations are bothersome, but not too severe. As desired luminosities continue to climb, however, polarization gradients will become an increasingly serious problem.

Looking forward, as mentioned toward the end of section IIA, polarization gradients are not the only challenge that will face future polarized  $^3\text{He}$  targets. These targets are well known to be prone to rupturing when they are used in an electron beam for extended periods of time. With care, by controlling wall thicknesses and densities, time periods of 5–6 weeks have become possible without losing a target, but targets have also been known to rupture within a few days. Since radiation damage is almost certainly playing a role, it will become necessary to take more precautions, including moving the pumping chamber (which must be transparent, and hence presumably glass) further from the beam. With a single transfer tube, such a change would result in very severe polarization gradients.

We present in this work a relatively simple solution to the two issues mentioned above. In a cell in which convection drives the mixing of gas between the cell's two chambers, as illustrated explicitly in Fig. 9, polarization gradients are quickly forced to near zero. Furthermore, the speed with which the gas is mixed can be varied quite independently of the separation between the cell's two chambers, thus making it possible to relocate the pumping chamber further from the electron beam. Finally, the fact that convective mixing can be accomplished in such a simple manner, with no moving parts or pumps, ensures that there is no need (at least associated with the convection) to introduce new materials that might cause excessive spin relaxation.

It is natural to ask just how much the performance of polarized  $^3\text{He}$  targets can be improved given current technology. More specifically, is it realistic to be consider-

ing increases in luminosity that would: 1) force the issue of polarization gradients to be addressed and 2) would force larger separations between the pumping and target chambers in order to avoid radiation damage? To better answer this question, we show below results from a bench test of a polarized  $^3\text{He}$  target cell that was constructed for use in an experiment (JLab E06-014) to measure a quantity known as  $d_2^n$ , a twist-three matrix element that is sensitive to the response of the color electric and magnetic fields to the neutron polarization [27]. This bench test involved a target cell similar in many ways to the cell Edna, although the diode-laser arrays that were used for optical pumping were spectrally-narrowed such that their line widths were about 10 times narrower than their broadband counterparts. As can be seen in Fig. 10, the polarization quickly climbed to values well above those shown in Fig. 2. Ultimately this cell achieved a polarization of slightly over 70%, significantly higher than the best performance we had previously observed for large target cells which reached the mid 50% range. In addition to the high polarization, the rate characterizing the spinup,  $\Gamma_s = (4.63 \text{ hrs})^{-1}$ , was even faster than the range of spinup rates that was assumed for Edna in Fig. 2. Using this value for  $\gamma_{su}$  in Eqn. 6 (which predicts  $P_{\text{He}}$  vs. beam current  $I$ ), we would expect Samantha to be even more tolerant to high beam current than was the case with Edna. Indeed, while the data from JLab E06-014 are still being analyzed, preliminary indications are that the target ran well above 60% even with 12  $\mu\text{A}$  of beam.

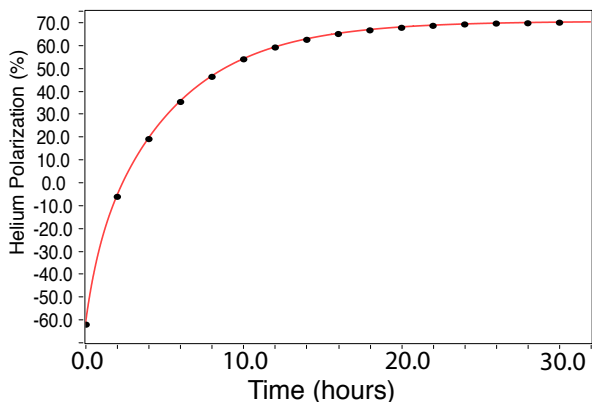


FIG. 10: Shown is polarization as a function of time for the cell “Samantha”, which was constructed for JLab experiment E06-014. A polarization of 70% was reached, a record for any polarized  $^3\text{He}$  target cell used for electron scattering.

In short, when alkali-hybrid SEOP is used in combination with high-power spectrally-narrowed diode-laser arrays, it becomes possible to build large polarized  $^3\text{He}$  targets that can achieve high polarization even in the presence of high beam currents. The one caveat is that with the current design, using a single transfer tube, polarization gradients become a limiting factor. Both alkali-hybrid SEOP and spectrally narrowed lasers contribute

to greater efficiency in the use of laser light, something that makes it possible to achieve significantly faster spin-exchange rates. The spectrally narrowed lasers also result in significantly higher alkali polarization, which translates into higher  $^3\text{He}$  polarization. The next generation of polarized  $^3\text{He}$  targets will be capable of running at very high beam currents, but only if the issue of polarization gradients can be brought under control.

In conclusion, with the advances in performance brought about by a combination of alkali-hybrid spin-exchange optical pumping and spectrally-narrowed diode-laser arrays, the point has been reached when it is desirable to explore target-cell geometries that go beyond that shown in Fig. 1. We suggest that the convection-based gas mixing demonstrated in this work can play an important role in implementing high-luminosity polarized  $^3\text{He}$  targets in the future. Not only will the use of convection reduce polarization gradients, it will also make it possible to have greater flexibility in the placement of the pumping chamber with respect to the target chamber. This flexibility can make possible, for example, the use of radiation shielding, and even the use of multiple pumping chambers. Convection-based polarized  $^3\text{He}$  target cells open multiple new possibilities that collectively address many of the challenges facing the next generation of high-luminosity polarized  $^3\text{He}$  targets.

## Appendix A: Solution to the Coupled Differential Equations

In order to solve Eqns. 7 and 8, it is useful to write them in the form

$$\dot{P}_{\text{pc}} = aP_{\text{pc}} + bP_{\text{tc}} + B \quad (\text{A1})$$

$$\dot{P}_{\text{tc}} = cP_{\text{pc}} + dP_{\text{tc}} \quad (\text{A2})$$

where  $a = -(\gamma_{\text{se}} + \Gamma_{\text{pc}} + d_{\text{pc}})$ ,  $b = d_{\text{pc}}$ ,  $c = d_{\text{tc}}$ ,  $d = -(\Gamma_{\text{tc}} + d_{\text{tc}})$  and  $B = \gamma_{\text{se}}P_{\text{A}}$ . The easiest way to solve these coupled differential equations is to decouple them, resulting in the equations:

$$\ddot{P}_{\text{pc}} - (a + d)\dot{P}_{\text{pc}} - (bc - ad)P_{\text{pc}} = -Bd \quad \text{and} \quad (\text{A3})$$

$$\ddot{P}_{\text{tc}} - (a + d)\dot{P}_{\text{tc}} - (bc - ad)P_{\text{tc}} = Bc \quad . \quad (\text{A4})$$

The solution to Eqn. A3 is given by

$$P_{\text{pc}}(t) = P_{\text{pc}}^g(t) + P_{\text{pc}}^p(t) \quad (\text{A5})$$

where  $P_{\text{pc}}^g(t)$  is the general solution and  $P_{\text{pc}}^p(t)$  is the particular solution. The general solution is found by solving

$$\ddot{P}_{\text{pc}} - (a + d)\dot{P}_{\text{pc}} - (bc - ad)P_{\text{pc}} = 0 \quad , \quad (\text{A6})$$

and is given by

$$P_{\text{pc}}^g(t) = c_{\text{pc}}^+ e^{\lambda^+ t} + c_{\text{pc}}^- e^{\lambda^- t} \quad (\text{A7})$$

where the eigenvalues,  $\lambda^\pm$  are given by

$$\lambda^\pm = \frac{1}{2} \left[ (a+d) \pm \sqrt{(a+d)^2 + 4(bc-ad)} \right] \quad (\text{A8})$$

$$= \frac{1}{2}(a+d) \left[ 1 \pm \sqrt{1 + \frac{4(bc-ad)}{(a+d)^2}} \right]. \quad (\text{A9})$$

These eigenvalues correspond to physical rates according to the following relationship

$$\Gamma_s = -\lambda^- \quad (\text{A10})$$

$$\Gamma_f = -\lambda^+ \quad (\text{A11})$$

where the subscripts  $s$  and  $f$  identify the two rates as slow and fast respectively.

The particular solution is easy to guess:

$$P_{\text{pc}}^p(t) = \frac{Bd}{bc-ad}. \quad (\text{A12})$$

The solution to Eqn. A3 is therefore

$$P_{\text{pc}}(t) = c_{\text{pc}}^+ e^{-\Gamma_s t} + c_{\text{pc}}^- e^{-\Gamma_f t} + \frac{Bd}{bc-ad}. \quad (\text{A13})$$

This can be simplified by defining the constraints

$$P_{\text{pc}}(t = \infty) = P_{\text{pc}}^\infty \quad (\text{A14})$$

$$\text{and } P_{\text{pc}}(t = 0) = P_{\text{pc}}^0. \quad (\text{A15})$$

Eqn. A14 is the particular solution,

$$P_{\text{pc}}^\infty = \frac{Bd}{bc-ad}. \quad (\text{A16})$$

Eqn. A15 gives

$$C_{\text{pc}} \equiv c_{\text{pc}}^+ = P_{\text{pc}}^0 - P_{\text{pc}}^\infty - c_{\text{pc}}^- . \quad (\text{A17})$$

Finally,

$$P_{\text{pc}}(t) = C_{\text{pc}} e^{-\Gamma_s t} + (P_{\text{pc}}^0 - P_{\text{pc}}^\infty - C_{\text{pc}}) e^{-\Gamma_f t} + P_{\text{pc}}^\infty. \quad (\text{A18})$$

The target chamber solution is found similarly (and has the same characteristic rates,  $\Gamma_s$  and  $\Gamma_f$ ),

$$P_{\text{tc}}(t) = C_{\text{tc}} e^{-\Gamma_s t} + (P_{\text{tc}}^0 - P_{\text{tc}}^\infty - C_{\text{tc}}) e^{-\Gamma_f t} + P_{\text{tc}}^\infty, \quad (\text{A19})$$

where

$$P_{\text{tc}}^\infty = -\frac{Bc}{bc-ad} = -\frac{c}{d} P_{\text{pc}}^\infty. \quad (\text{A20})$$

Finally,  $C_{\text{pc}}$  can be obtained by using Eqn. A18 to solve Eqn. A1 at  $t = 0$ ,

$$C_{\text{pc}} + (P_{\text{pc}}^0 - P_{\text{pc}}^\infty - C_{\text{pc}}) + P_{\text{pc}}^\infty = aP_{\text{pc}}^0 + bP_{\text{tc}}^0 + B, \quad (\text{A21})$$

$$\text{so } C_{\text{pc}} = \frac{\Gamma_s(P_{\text{pc}}^\infty - P_{\text{pc}}^0) - aP_{\text{pc}}^0 - bP_{\text{tc}}^0 - B}{\Gamma_f - \Gamma_s}. \quad (\text{A22})$$

Similarly,

$$C_{\text{tc}} = \frac{\Gamma_s(P_{\text{tc}}^\infty - P_{\text{tc}}^0) - cP_{\text{pc}}^0 - dP_{\text{tc}}^0}{\Gamma_f - \Gamma_s}. \quad (\text{A23})$$

## Appendix B: Estimate of the magnitude of flow in the convection cells.

Here we formulate estimates for the parameters that appear in Eqn. 43.

### 1. The viscosity of $^3\text{He}$

Since our temperatures are in the classical regime ( $T \gg 3K$ ), the viscosity of  $^3\text{He}$  can be calculated from the viscosity of  $^4\text{He}$  using [28].

$$\eta_{\text{He3}} = \sqrt{\frac{m_{\text{He3}}}{m_{\text{He4}}}} \eta_{\text{He4}} \quad (\text{B1})$$

$$= 0.8681 \eta_{\text{He4}}. \quad (\text{B2})$$

We parameterize the  $^4\text{He}$  viscosity in the range of 0 – 300°C using Kestin et al. [29],

$$\eta_{\text{He4}} = A + B \times T + C \times T^2 \quad (\text{B3})$$

where  $T$  has units of °C and

$$A = 18.82(2) \mu\text{Pa} \cdot \text{s}, \quad (\text{B4})$$

$$B = 0.0456(2) \mu\text{Pa} \cdot \text{s}/^\circ\text{C} \quad (\text{B5})$$

$$\text{and } C = -13.8(6) \mu\text{Pa} \cdot \text{s}/(^\circ\text{C})^2. \quad (\text{B6})$$

At 20°C,  $\eta_{\text{He3}} = 17.12 \mu\text{Pa} \cdot \text{s}$ .

The flow in a pipe is Laminar if the Reynold's number is below 2300 [30]. The Reynolds number is defined as

$$Re = \frac{2R\rho v}{\eta}, \quad (\text{B7})$$

where  $\rho$  is the density of the fluid. A pipe 1.2cm wide that is filled with 8 amagats  $^3\text{He}$  at 20°C ( $\rho \approx 1\text{kg}/\text{m}^3$ ) will have laminar flow provided  $v \ll 20000 \text{ cm}/\text{min}$ .

### 2. Flow in the Convection Cell

The flow in the convection cell arises from a forced density difference between the two transfer tubes – one tube is maintained at room temperature while the other is heated (see Fig. 6). Modeling the convection cell as five contiguous pipes, Eqn. 37 becomes

$$\Delta\rho gh 2\pi r dr = -2\pi \sum_i^5 \eta_i l_i \frac{d}{dr_i} \left( r_i \frac{dv_i}{dr_i} \right) dr_i \quad (\text{B8})$$

where  $h$  is the vertical length of transfer tube that is held at an elevated temperature (see Fig. 11). In this model we approximate the pumping chamber as a cylinder with transfer tubes entering axially, and identify five distinct regions in the cell as is indicated in Fig. (11). Each region is identified as a pipe of length  $l_i$ , radius  $R_i$  and temperature  $T_i$ . We further assume that  $T_1 = T_4$ ,  $T_3 = T_5$

and  $R_1 = R_2 = R_3$ . Finally, we identify  $T_C \equiv T_1$  and  $T_H \equiv T_2$ . We note that both the density and viscosity of the gas are temperature dependent.

The continuity equation,  $\rho_j A_j v_j = \rho_i A_i v_i$  and some distance rescaling provide further simplification,

$$v_i = \frac{\rho_1 R_1^2}{\rho_i R_i^2} v_1, \quad (\text{B9})$$

$$r_i = \frac{R_i}{R_1} r_1 \quad (\text{B10})$$

$$\text{and } \frac{d}{dr_i} = \frac{R_1}{R_i} \frac{d}{dr_1}. \quad (\text{B11})$$

Since  $v_i$  and  $r_i$  have been expressed in terms of  $v_1$  and

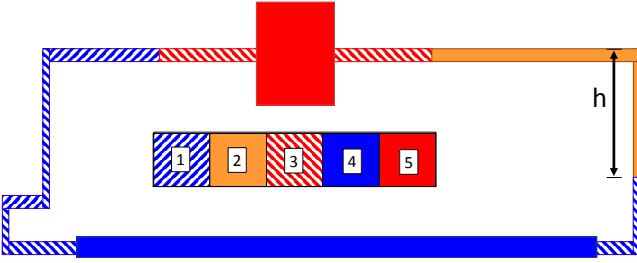


FIG. 11: Diagram indicating the different temperature regions used to describe the convection cell.

$r_1$ , we'll drop their subscripts. Finally,

$$v(r) = \frac{1}{4} \frac{\Delta \rho g h (r^2 - R_1^2)}{\eta_1 \left( l_1 + l_4 \frac{R_1^2}{R_4^2} \right) + \eta_2 l_2 \frac{\rho_1 R_1^2}{\rho_2 R_2^2} + \eta_3 \frac{\rho_1}{\rho_3} \left( l_3 \frac{R_1^2}{R_3^3} + l_5 \frac{R_1^2}{R_5^2} \right)} \quad (\text{B12})$$

Eqn. (B12) assumes that there are no “minor losses” in the system, where a minor loss represents a pressure drop due to a sudden change in flow from a pipe fitting or a pipe expansion or contraction; the term “minor loss” refers to a loss that is small relative to the overall length of pipe under consideration [25, 31]. In our case, due to the relatively short length of the cell, the minor losses are actually significant. The actual cell, Fig. (6) consists of four elbow bends, two tees, and four expansions/contractions. The retarding forces these losses exert on the gas can be approximated by considering instead an equivalent length of straight pipe.

The expansions/contractions have a relatively small loss, which is equivalent in magnitude to the loss that would be incurred passing through a pipe of length [31]

$$L_{equivalent} = \frac{2RK}{f}, \quad (\text{B13})$$

where  $R$  is the tube radius,  $f$  is the friction factor ( $f = 64/Re$  for laminar flow) and  $K$  is the fluid-independent resistance coefficient. For sudden expansions/contractions,

$$K_{expansion} = \left( 1 - \frac{r_{small}^2}{r_{large}^2} \right)^2 \quad (\text{B14})$$

$$\text{and } K_{contraction} = \frac{1}{2} \left( 1 - \frac{r_{small}^2}{r_{large}^2} \right)^2. \quad (\text{B15})$$

Gas flowing through the transfer tube/target chamber junction has  $K_{contraction} \approx 0.18$ ,  $K_{expansion} \approx 0.35$ . At  $v = 60 \text{ cm/min}$  ( $Re \approx 10$ ), this gives a negligible  $L_{equivalent} \approx 0.1 \text{ cm}$  – gas flowing between the pumping chamber and the transfer tube will have an even smaller  $L_{equivalent}$ .

The losses in the bends, however, are much greater. We model the loss coefficient in the bends using the 3-K method of Darby [32],

$$K = \frac{K_1}{Re} + K_i \left( 1 + \frac{K_d}{D^{0.3}} \right) \quad (\text{B16})$$

where  $D$  is the diameter of the pipe (in inches) and  $K_1, K_i, K_d$  are geometry-dependent loss coefficients. We approximate our glass bends as flanged, welded bends with  $r_b/D = 2$  (here,  $r_b$  is the radius of the bend); such bends have  $K_1 = 800, K_i = 0.056, K_d = 3.9$ . For laminar flow, the 3-K method gives

$$L_{equivalent} = \frac{2R}{64} \left[ K_1 + Re K_i \left( 1 + \frac{K_d}{D^{0.3}} \right) \right] \quad (\text{B17})$$

We treat the transfer tube/target chamber tee junctions as elbows (effectively ignoring the dead-end branch of the tee). The system therefore has five bends in temperature-region 1 (which have a total equivalent length of approximately 63 cm) and one bend in temperature-region 2 (which has an equivalent length of approximately 13 cm). Finally, using Eqn. 40 for  $\Delta \rho$  we find

$$v(r) = \frac{\frac{1}{4} (r^2 - R_1^2) \rho h g T_C \left( \frac{1}{T_C} - \frac{1}{T_H} \right)}{\eta_1 \left( l'_1 + l_4 \frac{R_1^2}{R_4^2} \right) + \eta_2 l'_2 \frac{\rho_1 R_1^2}{\rho_2 R_2^2} + \eta_3 \frac{T_3}{T_1} \left( l_3 \frac{R_1^2}{R_3^3} + l_5 \frac{R_1^2}{R_5^2} \right)} \quad (\text{B18})$$

where

$$l'_1 = l_1 + 5 \times \frac{2R_1}{64} \left[ K_1 + Re_1 K_i \left( 1 + \frac{K_d}{D_1^{0.3}} \right) \right] \quad (\text{B19})$$

$$l'_2 = l_2 + \frac{2R_2}{64} \left[ K_1 + Re_2 K_i \left( 1 + \frac{K_d}{D_2^{0.3}} \right) \right] \quad (\text{B20})$$

Note that the Reynold's number is dependent on the velocity of the gas.

Table B 2 lists values for  $R$  and  $l$ . Measurements of  $R$  (which is the inner diameter of the tube) require a knowledge of the thickness of the glass tube. We measured the thickness of the glass by observing interference patterns using a scannable single-frequency laser. Using this information, Eqn. B18 predicts velocities that agree within 20% of the measured value (see Fig. 8).

The maximum velocity in Eqn. B18 (corresponding to  $r = 0$ ) can be written as

$$v_{max} = \frac{\mathcal{A} \left( \frac{1}{T_{coldtt}} - \frac{1}{T_{hottt}} \right)}{1 + \beta(\Delta T)} \quad (\text{B21})$$

| R1   | R2   | R3   | R4   | R5    | h    | l1    | l2    | l3    | l4    | l5  |
|------|------|------|------|-------|------|-------|-------|-------|-------|-----|
| .498 | .521 | .502 | .806 | 4.034 | 4.76 | 24.99 | 20.87 | 15.18 | 40.32 | 5.6 |

TABLE I: Best Guesses for Convection Cell Dimensions (cm)

where

$$\Delta T = T_H - T_C, \quad (\text{B22})$$

$$\mathcal{A} = \frac{R_1^2 \rho h g T_C}{4 k_{\eta} \mathcal{L}}, \quad (\text{B23})$$

$$\beta = \beta_1 \Delta T + \beta_2 (\Delta T)^2 + \beta_3 (\Delta T)^3, \quad (\text{B24})$$

$$k_{\eta} \mathcal{L} = \eta_1 \left( l'_1 + l_4 \frac{R_1^2}{R_4^2} \right) + \eta_2 l'_2 \frac{\rho_1 R_1^2}{\rho_2 R_2^2} + \eta_3 \frac{T_3}{T_1} \left( l_3 \frac{R_1^2}{R_3^2} + l_5 \frac{R_1^2}{R_5^2} \right), \quad (\text{B25})$$

$$\Delta T = T_2 - T_1, \quad (\text{B26})$$

$$\beta_1 = l'_2 \frac{R_1^2}{R_2^2} \left[ \frac{\eta_1}{T_1} + 0.8681 (B + 2C(T_1 - 273)) \right], \quad (\text{B27})$$

$$\beta_2 = 0.8681 l'_2 \frac{R_1^2}{R_2^2} \left[ \frac{B + 2C(T_1 - 273)}{T_1} + C \right] \quad (\text{B28})$$

and (B29)

$$\beta_3 = 0.8681 l'_2 \frac{R_1^2}{R_2^2} \left[ \frac{C}{T_1} \right]. \quad (\text{B30})$$

In the above equations, all temperatures are in Kelvin.

Evaluating the above equations in terms of our best guesses for cell dimensions and temperatures, with  $T_C = 24.5^\circ\text{C}$  gives  $\mathcal{A} = 9.14 \times 10^4 \text{K}\cdot\text{cm}/\text{min}$ ,  $\beta_1 = 1.03 \times 10^{-3}$ ,  $\beta_2 = 1.26 \times 10^{-6}$ , and  $\beta_3 = -4.26 \times 10^{-10}$ . It is clear from these values that it is quite reasonable to neglect the terms involving  $\beta_2$  and  $\beta_3$ , which results in Eqn. 43 from section III-B.

- 
- [1] P. L. Anthony, R. G. Arnold, H. R. Band, H. Borel, P. E. Bosted, V. Breton, G. D. Cates, T. E. Chupp, F. S. Dietrich, J. Dunne, et al., *Phys. Rev. Lett.* **71**, 959 (1993).
- [2] Riordan and *et al.*, *Phys. Rev. Lett.* **105**, 262302 (2010).
- [3] K. P. Coulter, T. E. Chupp, A. B. McDonald, C. D. Bowman, J. D. Bowman, J. J. Szymanski, V. Yuan, G. D. Cates, D. R. Benton, and E. D. Earle, *Nuclear Instruments and Methods in Physics Research Section A: Accelerators, Spectrometers, Detectors and Associated Equipment* **288**, 463 (1990).
- [4] M. S. Albert, G. D. Cates, B. Driehuys, W. Happer, B. Saam, C. S. Springer, and A. Wishnia, *Nature* **370**, 199 (1994).
- [5] H. Middleton, R. D. Black, B. T. Saam, G. D. Cates, G. P. Cofer, R. Guenther, W. Happer, L. W. Hedlund, G. A. Johnson, K. Juvan, et al., *Magnetic Resonance in Medicine* **33**, 271 (1995).
- [6] F. Colegrove, L. Schearer, and G. Walters, *Physical Review* **132**, 2561 (1963).
- [7] P. Nacher and M. Leduc, *Journal de Physique* **46**, 2057 (1985).
- [8] M. Bouchiat, T. Carver, and C. Varnum, *Physical Review Letters* **5**, 373 (1960).
- [9] N. Bhaskar, W. Happer, and T. McClelland, *Physical Review Letters* **49**, 25 (1982).
- [10] T. E. Chupp, M. E. Wagshul, K. P. Coulter, A. B. McDonald, and W. Happer, *Phys. Rev. C* **36**, 2244 (1987).
- [11] J. Krimmer, M. Distler, W. Heil, S. Karpuk, D. Kiselev, Z. Salhi, and E. Otten, *Nuclear Instruments and Methods in Physics Research Section A: Accelerators, Spectrometers, Detectors and Associated Equipment* **611**, 18 (2009).
- [12] T. E. Chupp, R. A. Loveman, A. K. Thompson, A. M. Bernstein, and D. R. Tieger, *Phys. Rev. C* **45**, 915 (1992).
- [13] W. Happer, G. Cates, M. Romalis, and C. Erickson, *U.S. Patent No. 6,318,092* (2001).
- [14] E. Babcock, I. Nelson, S. Kadlecck, B. Driehuys, L. W. Anderson, F. W. Hersman, and T. G. Walker, *Phys. Rev. Lett.* **91**, 123003 (2003).
- [15] E. Babcock, B. Chann, T. G. Walker, W. C. Chen, and T. R. Gentile, *Phys. Rev. Lett.* **96**, 083003 (2006).
- [16] K. D. Bonin, T. G. Walker, and W. Happer, *Phys. Rev. A* **37**, 3270 (1988).
- [17] K. D. Bonin, D. P. Saltzberg, and W. Happer, *Phys. Rev. A* **38**, 4481 (1988).
- [18] *Nuclear Instruments and Methods in Physics Research Section A: Accelerators, Spectrometers, Detectors and Associated Equipment* **276**, 29 (1989), ISSN 0168-9002.
- [19] I. Kominis, Ph.D. thesis, Princeton University (2001).
- [20] A. Abragam, *Principles of Nuclear Magnetism* (Oxford University Press, 1961).
- [21] M. Romalis, Ph.D. thesis, Princeton University (1997).
- [22] X. Zheng, Ph.D. thesis, M.I.T. (2002).
- [23] J. Kestin, K. Knierim, E. A. Mason, B. Najafi, S. T. Ro, and M. Waldman, *J. Phys. Chem. Ref. Data* **13** (1984).
- [24] M. V. Romalis and G. D. Cates, *Phys. Rev. A* **105**, 3004 (1998).
- [25] R. Dodge and M. Thompson, *Fluid Mechanics* (McGraw-Hill Book Company, INC., 1937).
- [26] D. Tritton, *Physical Fluid Dynamics* (Van Nostrand Reinhold Company, Ltd., 1977).
- [27] Z.-E. Meziani, *Jefferson Laboratory Proposal E06-014* (2006).
- [28] W. E. Keller, *Phys. Rev.* **105**, 41 (1957).
- [29] J. Kestin, K. Knierim, E. Mason, B. Najafi, S. Ro, and M. Waldman, *J. Phys. Chem. Ref. Data* **13**, 229 (1984).
- [30] L. Schiller, *Forschungsarbeiten Ver. deut. Ing.* **248** (1922).
- [31] *Flow of fluids through valves, fittings, and pipe*, Technical Paper No. 410 (Crane Company, 2009).
- [32] R. Darby, *Chemical Engineering Fluid Mechanics* (Marcel Dekker, Inc., 2001).